Dalton
Transactions

An international journal of inorganic chemistry

Accepted Manuscript

This article can be cited before page numbers have been issued, to do this please use: A. Yardan, *Dalton Trans.*, 2026, DOI: 10.1039/D6DT00722H.

Dalton
Transactions

An international journal of inorganic chemistry
rsc.li/dalton

Volume 46
Number 10
14 March 2017
Pages 3073-3412

ISSN 0306-0012

ROYAL SOCIETY
OF CHEMISTRY

COMMUNICATION
Douglas W. Stephen *et al.*
N-Heterocyclic carbene stabilized parent sulfenyl, selenenyl, and tellurenyl cations (XH^+; X = S, Se, Te)

ROYAL SOCIETY
OF CHEMISTRY

rsc.li/dalton

View Article Online
DOI: 10.1039/D6DT00722H

A Ligand in the Metal Salt Sea: Extreme Metal-to-Ligand Ratios and the Thermodynamic Driving Force of the Halogen Bond

Alper Yardan

KEYWORDS: Extreme Stoichiometry, Ab Initio PXRD, Bailar Twist, Asymmetric Charge Transfer, Halogen Bonding, Spin Density

Abstract

This study presents the rational design, synthesis, and comprehensive structural elucidation of a novel series of halogenated coordination complexes featuring Cu(II), Co(II), Cd(II), and Mn(II) centers. By deliberately employing an extreme 10:1 metal-to-ligand stoichiometry, a supersaturated "metal salt sea" was successfully navigated to kinetically trap unique microcrystalline solid-state phases. Overcoming the inherent challenges of single-crystal growth, the intricate 3D architectures of these rapid-precipitation products were determined *ab initio* utilizing Powder X-ray Diffraction (PXRD) methodologies. Crystallographic analyses reveal a striking structural diversity, notably featuring highly asymmetric binuclear cores. The immense steric encumbrance of the chelating counter-anions forces the metal centers into unusual coordination environments, including a severely distorted 6-coordinate intermediate trapped along the Bailar twist pathway (between O_h and D_{3h} geometries), alongside a validated square-pyramidal distortion ($\tau_5 = 0.303$). Crucially, Quantum Theory of Atoms in Molecules (QTAIM) and Non-Covalent Interaction (NCI) analyses unmasked a highly localized Br···O halogen bond acting as a potent thermodynamic anchor (~6.25 kcal/mol), overriding classical steric expectations to dictate the ultimate coordination topology. Alongside this, Frontier Molecular Orbital (FMO) and 3D spin density mapping uncovered profound intramolecular electronic communication, revealing distinct Ligand-to-Metal Charge Transfer (LMCT) pathways and robust superexchange mechanisms. Translating these molecular-level interactions to macroscopic properties, morphological investigations via Transmission Electron Microscopy (TEM) revealed a spectacular, metal-dependent nanoscale evolution. The macroscopic morphologies ranged from ultra-thin (~5 nm) 1D nanowires—strictly dictated by Jahn-Teller distortions—and uniform nanorods to polymorphic networks, sub-50 nm polymeric clusters, and massive aggregates featuring sponge-like interstitial cavities. Finally, Thermogravimetric Analysis (TGA) demonstrated the remarkable thermal stability (up to 400–500 ˚C) of these robust networks. The flawless synergy between empirical structural models, theoretical simulations, and physicochemical characterizations provides profound insights into the predictive engineering of hierarchical supramolecular materials via extreme concentration gradients.

View Article Online
DOI: 10.1039/D6DT00722H

Introduction

In the conventional landscape of coordination chemistry, organic ligands typically interact with metal salts in balanced, stoichiometric harmony.[1,2] In contrast, when a flexible ligand is submerged in a vast, supersaturated "sea" of metal salts, the classical rules of coordination are profoundly challenged. Under such extreme concentration gradients, the counter-anions—traditionally relegated to the role of passive charge-balancing spectators in the outer coordination sphere—are forced to act as aggressive structural directors.[3,4] To explore this phenomenon, Schiff base ligands containing O, N, O donor sets, particularly those derived from ethanolamine derivatives, serve as exceptional molecular probes due to their remarkable conformational flexibility and their ability to adapt to severe coordination stress. Moreover, the coordination chemistry of such N/O-donor ligands with versatile transition metals like Cu(II), Mn(II), Co(II), and Cd(II) remains a highly active field, driven by their diverse structural topologies and broad applications in modern chemical sciences.[5]

In previous studies by the author, versatile Schiff base frameworks were successfully utilized to construct diverse supramolecular topologies, ranging from complex heterodinuclear and heterotrinuclear assemblies to one-dimensional polymeric zig-zag copper(II) chains.[6-8] These earlier investigations clearly demonstrated that under standard stoichiometric reaction conditions (e.g., 1:1 or 1:2 metal-to-ligand ratios), the rational design of the ligand backbone primarily dictates the final nuclearity and topology of the resulting coordination compounds. In such conventional synthetic regimes, the counter-anions of the metal salts typically act as simple charge-balancing spectators, often remaining in the outer coordination sphere and playing only secondary roles in the overall crystal packing.

However, the structural role of these counter-anions can be dramatically altered by deliberately perturbing the reaction environment. It was hypothesized that subjecting the ligand to a highly saturated "metal salt sea"—specifically by applying an extreme metal-to-ligand ratio (10:1)—would create a significant coordination stress. Under such extreme stoichiometric conditions, the typically non-coordinating or spectator anions are forced to directly participate in the primary coordination sphere, thereby exerting a strong structure-directing (templating) effect.

In this contribution, the synthesis and comprehensive structural elucidation of a series of novel transition metal complexes (Cu(II), Co(II), Cd(II), and Mn(II)) engineered under these extreme concentration regimes are presented. By employing a diverse set of metal salts (nitrates, sulfates, acetates, and chlorides) against a single versatile Schiff base ligand, an extraordinary anion-directed structural diversity is showcased. The resulting architectures were rigorously characterized using powder X-ray diffraction (PXRD) coupled with Rietveld refinement, FT-IR spectroscopy, thermal analysis (TGA), and transmission electron microscopy (TEM). These experimental structural findings are further deeply corroborated and expanded upon by high-level Density Functional Theory (DFT) calculations, including Molecular Electrostatic Potential (MEP) mapping, Frontier Molecular Orbital (FMO) analysis, and 3D spin density evaluations. These advanced computational studies go beyond mere structural validation to unveil the intricate intramolecular electronic communication, directional Ligand-to-Metal

View Article Online
DOI: 10.1039/D6DT00722H

Charge Transfer (LMCT) pathways, and robust magnetic super-exchange mechanisms governing these complexes. Ultimately, the theoretical identification of specific supramolecular synthons—such as halogen-bonded σ-holes and highly polarized electrostatic domains—provides a profound, unambiguous rationale for the extraordinary hierarchical self-assembly observed morphologically, bridging the gap between sub-nanometer quantum chemistry and macroscopic 3D architectures.[9-11]

Beyond the primary coordination sphere, the ultimate 3D crystal packing of these highly distorted networks is governed by subtle yet powerful non-covalent interactions. While halogen bonding, driven by the highly directional electropositive σ-hole, has emerged as a crucial tool in supramolecular chemistry, quantifying its thermodynamic contribution in such extreme metal-to-ligand stoichiometries remains scarce. Evaluating the precise role of these non-covalent interactions from a coordination chemistry perspective requires rigorous theoretical support; hence, DFT calculations have become fundamentally important for unraveling the energetic and electronic nature of σ-hole driven assemblies.[12] Therefore, alongside *ab initio* structural elucidation via PXRD, this study systematically employs advanced computational tools—including Molecular Electrostatic Potential (MEP), Quantum Theory of Atoms in Molecules (QTAIM), and Non-Covalent Interaction (NCI) analyses—to unmask and quantify the thermodynamic driving forces of the supramolecular anchors dictating these unique architectures.

View Article Online
DOI: 10.1039/D6DT00722H

Results and Discussion

Synthesis and Spectroscopic (IR) Features

Table 1. Complexes and Formulas

Complex Formula	**Molecule Formula**	**Complex Number**
$[Cu(HL)(NO_3)]$	$C_9H_9BrCuN_2O_5$	**1**
$[Co(H_2L)_2](NO_3)_2$	$C_{18}H_{20}Br_2CoN_4O_{10}$	**2**
$[Mn(HL)(Cl)(H_2O)]\cdot H_2O$	$C_9H_{13}BrClMnNO_4$	**3**
$[Cu_2(HL)_2(\mu\text{-}SO_4)]$	$C_{18}H_{18}Br_2Cu_2N_2O_8S$	**4**
$[Cd_2(HL)_2(NO_3)_2]_n$	$(C_{18}H_{18}Br_2Cd_2N_4O_{10})_n$	**5**
$[Co_2(HL)_2(\mu\text{-}OAc)_2]$	$C_{22}H_{24}Br_2Co_2N_2O_8$	**6**

The assigned empirical formulas and corresponding structural numbering (1–6) of the isolated complexes are summarized in **Table 1**. Subsequently, the final Rietveld refinements for all complexes (detailed in **Table 2**) converged to excellent agreement factors, confirming the phase purity, the crystallographic parameters, and the accuracy of the proposed structural models.

View Article Online
DOI: 10.1039/D6DT00722H

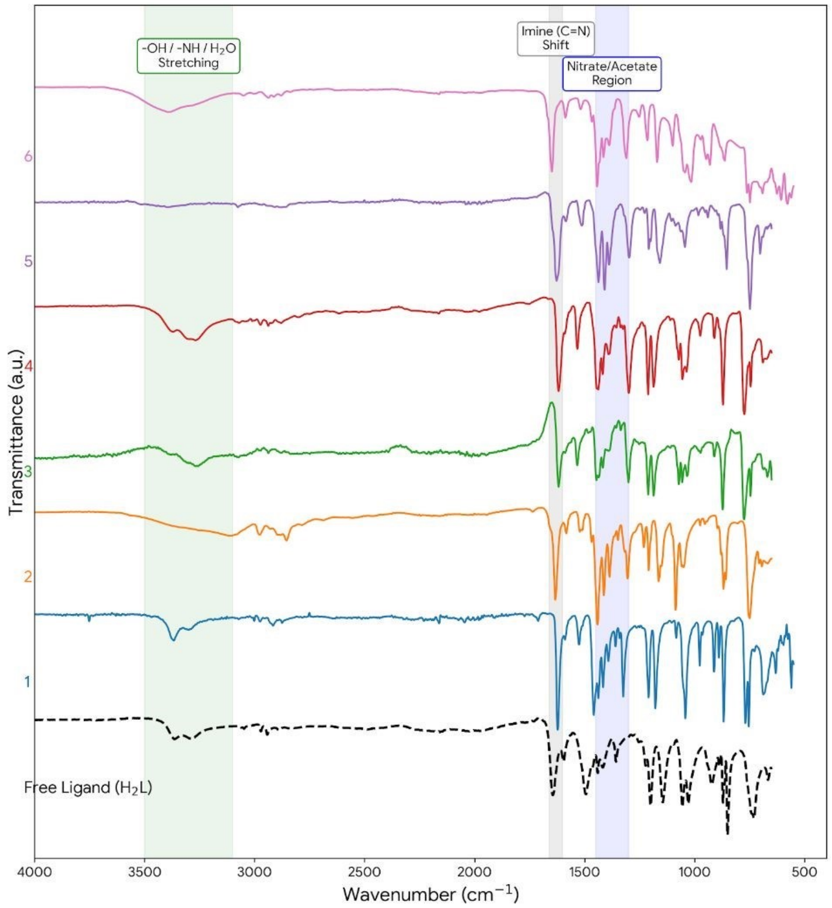

Figure 1. Solid-state FT-IR stacked spectra of the free ligand (H_2L) and its respective metal complexes (1-6). The colored vertical bands highlight the diagnostic shifting of the imine (*C=N*) stretching frequencies upon metal coordination (gray), the distinctive anisobidentate/bridging vibration modes of the counter-anions (blue), and the broad stretching regions corresponding to the conserved uncoordinated aliphatic –OH protons, –NH groups, and lattice/coordinated water molecules (green)

The implementation of an extreme 10:1 (metal-to-ligand) stoichiometric ratio profoundly altered the conventional reaction kinetics, triggering the rapid and near-instantaneous precipitation of microcrystalline solid-state phases. This supersaturated 'metal salt sea' effectively kinetically trapped the complexes, circumventing standard thermodynamic equilibrium pathways. The coordination modes of these kinetically trapped species were initially elucidated via FT-IR spectroscopy. As comparatively illustrated in the stacked spectra (**Figure 1**), a diagnostic shift in the imine stretching frequency confirmed the active participation of the Schiff base nitrogen in metal coordination across all complexes.[14] Additionally, the spectra distinctly fingerprinted the coordination nature of the counter-anions.

View Article Online
DOI: 10.1039/D6DT00722H

For instance, the Cu(II)-nitrate complex (**1**) exhibited a pronounced asymmetric stretching splitting (134 cm^{-1}), highly characteristic of an anisobidentate nitrate coordination. Conversely, the Co(II)-acetate complex (**6**) displayed distinct symmetric and asymmetric carboxylate stretching vibrations indicative of a bridging coordination mode, foreshadowing its binuclear dimeric architecture.[15]

Structural Diversity Directed by Anions and Quantum Chemical Insights

The conventional stoichiometric synthesis of transition metal complexes with multidentate Schiff base ligands typically yields discrete, low-nuclearity species where counter-anions remain as uncoordinated spectators. However, the employed supersaturated (10:1) synthetic strategy radically altered this paradigm, forcing the typically passive anions into the primary coordination sphere. This severe coordination stress resulted in an extraordinary structural diversity. Depending entirely on the coordinating nature of the specific counter-anion, the supramolecular topology transitioned through a complete hierarchical spectrum: from discrete 0D monomers (e.g., Cu (**1**) and Mn (**3**) complexes) to isolated 0D binuclear dimers (e.g., Cu-sulfate (**4**) and Co-acetate (**6**)).

Structural Elucidation via Ab Initio Powder X-Ray Diffraction

To unambiguously determine the 3D solid-state architectures of the microcrystalline powders, structure solutions were performed directly from high-resolution PXRD data utilizing the simulated annealing algorithm within the EXPO2014 software suite. Subsequent model optimizations were achieved via rigid-body Rietveld refinement. Given the inherent nature of direct-space powder methods, minor computational artifacts, such as geometric H···H short contacts at the unit cell boundaries, are expected consequences of the riding model optimization and do not compromise the rigorous integrity of the heavy-atom skeletons.[15] The final Rietveld refinements for all complexes (summarized in **Table 2**) converged to excellent agreement factors, confirming the phase purity and the accuracy of the proposed structural models.

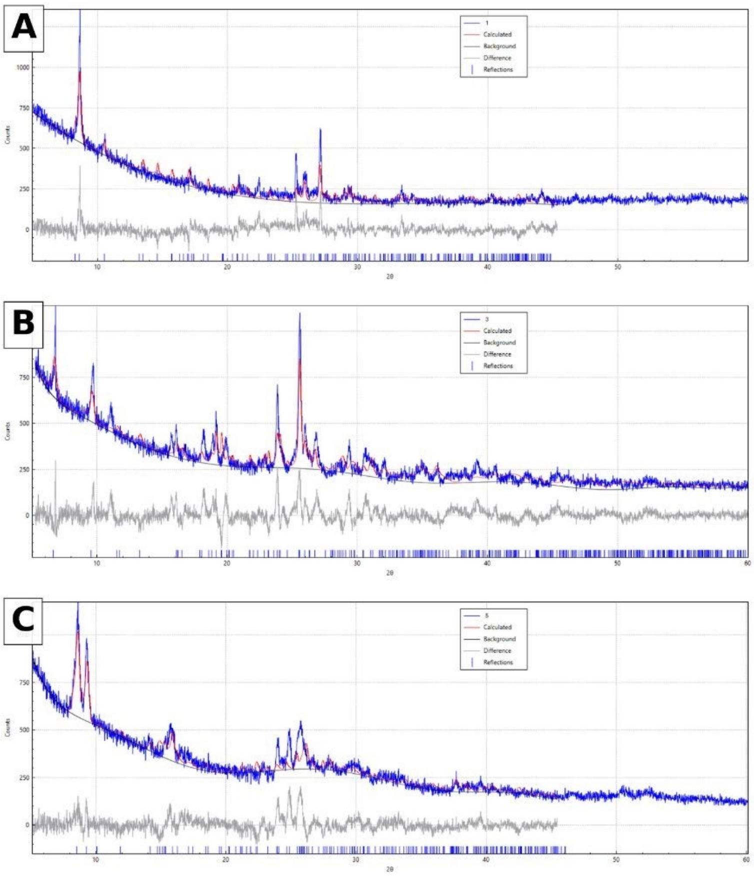

Figure 2. Final Rietveld refinement profiles for the representative microcrystalline architectures. (A) The strongly Jahn-Teller distorted mononuclear Cu(II) complex (1). (B) The highly hydrated mononuclear Mn(II) complex (3). (C) The asymmetric binuclear Cd(II) dimer (5). The experimental PXRD data are shown as blue circles, the calculated patterns as red solid lines, and the difference profiles (experimental minus calculated) as grey solid lines at the bottom. Blue vertical tick marks indicate the calculated Bragg reflection positions. The exceptionally flat difference profiles visually and statistically validate the high accuracy of the *ab initio* direct-space structure solutions.

The exceptional quality of these crystallographic fits is visually corroborated by the remarkably flat difference profiles in the final Rietveld plots, as representatively showcased for the mononuclear Cu(II) (**1**), Mn(II) (**3**), and binuclear Cd(II) (**5**) complexes (**Figure 2**). The primary coordination spheres of the isolated architectures exhibit remarkable geometric diversity. As

View Article Online
DOI: 10.1039/D6DT00722H

highlighted in the comparative polyhedral representations (**Figure 3**), the structural landscape ranges from pronounced Jahn-Teller axially elongated monomers (**1**) to striking crystallographic asymmetries within the binuclear cores (**5** and **6**).[16] For the **6**, a relatively high background was observed in the PXRD pattern due to the strong secondary fluorescence of Cobalt under Cu-K\α radiation, which is inherently reflected in the Bragg R-factors despite the excellent overall profile fit (R_{wp} = 5.7%).

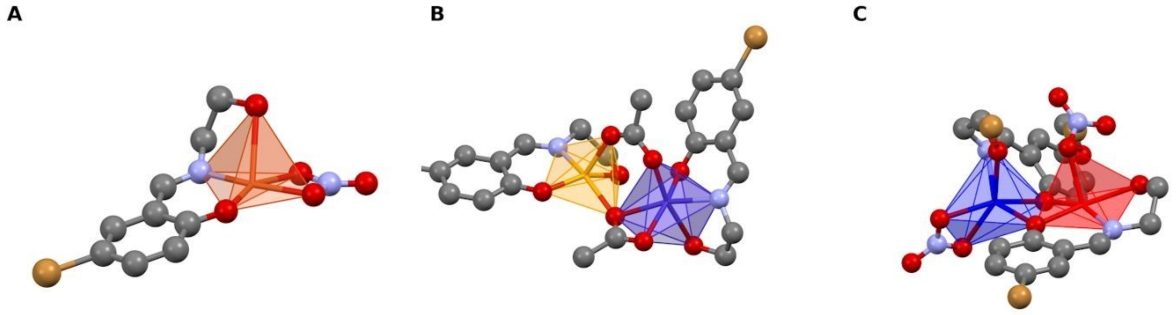

Figure 3. Polyhedral representations illustrating the diverse primary coordination spheres and geometric distortions of the synthesized complexes. **(A)** The mononuclear Cu(II)-nitrate complex (**1**), displaying a pronounced Jahn-Teller axial elongation characteristic of its d^9 electronic configuration. **(B)** The binuclear Co(II)-acetate dimer (**6**) and **(C)** the Cd(II)-nitrate dimer (**5**). Both multinuclear architectures highlight a striking crystallographic asymmetry, showcasing the coexistence of highly distinct coordination environments within the binuclear cores. These specifically include validated square-pyramidal geometries alongside severely distorted 6-coordinate centers trapped along the Bailar twist pathway (representing an intermediate between ideal O_h and D_{3h} topologies), strictly driven by competitive counter-anion coordination and immense steric constraints.

Table 2. Crystallographic data and Rietveld refinement parameters for complexes 1–6 obtained *ab initio* from PXRD analysis.

	1	**2**	**3**	**4**	**5**	**6**
MW	368.63	547.11	369.50	709.30	834.99	722.12
Crystal System	Triclinic	Triclinic	Triclinic	Triclinic	Triclinic	Triclinic
Space Group	$P\bar{1}$	$P\bar{1}$	$P\bar{1}$	$P\bar{1}$	$P1$	$P\bar{1}$
a (Å)	11.122(5)	19.458(4)	13.709(4)	17.159(4)	11.111(4)	14.460(4)
b (Å)	10.569(4)	14.756(3)	11.736(3)	10.599(3)	10.209(3)	11.852(3)

c (Å)	6.673(2)	11.538(3)	6.053(2)	10.619(3)	7.450(2)	10.563(3)
α (deg)	94.65(3)	108.61(2)	103.06(3)	106.10(2)	89.93(2)	104.86(2)
β (deg)	100.52(2)	109.18(2)	99.84(2)	90.51(2)	93.63(2)	104.94(2)
γ (deg)	76.57(5)	101.57(2)	95.33(3)	107.93(2)	68.89(3)	87.03(2)
Volume ($Å^3$)	749.5(5)	2787.2(5)	925.9(5)	1755.8(5)	786.6(5)	1690.6(5)
Z, Z'	2, 1	2, 1	2, 1	2, 1	1, 1	2, 1
R_{WP} (%)	10.39	9.21	8.91	14.45	6.91	5.70
R_P (%)	7.42	6.68	6.86	10.45	5.40	4.51
GOF	2.76	2.16	1.53	2,87	1.47	1.49

Monomeric Architectures: Cu(II)-Nitrate (1), Co(II)-Nitrate (2), and Mn(II) (3) Complexes

Driven by the severe concentration gradients, the (**1**) and (**3**) complexes crystallized as discrete 0D monomers in the triclinic $P\overline{1}$ space group. The central Cu(II) ion adopts a square pyramidal geometry characterized by a strong equatorial plane and a notably elongated axial Cu-O(alcohol) bond (2.558 Å). This distinct axial elongation provides direct physical evidence of the pronounced Jahn-Teller distortion inherent to the d^9 configuration.[17] The packing is tightly governed by highly directional Br···O (2.71 Å) halogen bonds—where the bromine σ-hole acts as a potent Lewis acid—forming a stable supramolecular network with intrinsic solvent-accessible micro-channels (approx. 188 $Å^3$).

Similarly, the Mn(II) monomer incorporates both a coordinated aqua ligand and uncoordinated lattice water molecules. These hydration spheres synergistically act as structural directors, engaging in an extensive intermolecular hydrogen-bonding network (O–H···O: 2.64–2.99 Å)

View Article Online
DOI: 10.1039/D6DT00722H

that stabilizes a highly fascinating microporous architecture containing substantial void spaces (245 Å³, approx. 26% of the unit cell).

In addition, the Co(II)-nitrate complex crystallizes as a discrete mononuclear entity. Conversely, its uncoordinated outer-sphere nitrate anions drive a highly specific charge-assisted hydrogen bonding network, acting as the fundamental supramolecular glue for its extended macroscopic assembly.

Binuclear Dimeric Architectures: Cu(II)-Sulfate (4), Cd(II) (5) and Co(II)-Acetate (6)

The structural landscape evolved dramatically with the introduction of bridging counter-anions, leading to the formation of highly stable 0D binuclear (dimeric) cores. A striking feature across the Cd(II) and Co(II) dimers is the formation of highly asymmetric binuclear cores, where the two metal centers exhibit crystallographically distinct coordination environments. This phenomenon highlights a rigorous steric packing frustration during the rapid crystallization process.[18] The 6-coordinate metal centers exhibit severely distorted coordination geometries. The profound structural deformation is quantitatively evidenced by the massive deviations of the *cis* angles (ranging widely from 55.85° to 113.37°), where the highly acute angle of 55.85° arises directly from the restricted bite angle of the chelating bidentate nitrate group. More importantly, the *trans* axes are significantly bent away from ideal linearity, ranging from 136.21° to 158.34°. This severe bending indicates that the coordination polyhedron is heavily distorted along the Bailar twist pathway, representing a highly constrained structural intermediate trapped between the ideal octahedral (O_h) and trigonal-

View Article Online
DOI: 10.1039/D6DT00722H

prismatic (D_{3h}) geometries. Such a dramatic topological shift is a direct consequence of the immense steric encumbrance imposed by the supramolecular bridging network.

The dimerization is robustly mediated by μ-phenoxo bridging mechanisms originating from the ligand backbone, a classic structural motif in multinuclear Schiff base chemistry.[19] In the Cu(II)-sulfate complex, this architecture is uniquely reinforced by a dual-bridging system where both the phenoxo oxygen and a sulfate oxygen exhibit a μ_3-coordination mode, creating a tightly locked binuclear core rarely observed in such saturated metal-salt environments.

Compared to standard 1:1 or 1:2 stoichiometric syntheses in the literature, which typically yield highly symmetric species with passive spectator anions,[20,21] the novelty of our 10:1 supersaturation approach lies in its ability to force severe coordination stress. This uniquely allows the highly electropositive bromine σ-hole to act as a supramolecular anchor, kinetically trapping rare, highly asymmetric structures—such as the Bailar twist intermediate—which remain largely undocumented in conventional halogen-bonded coordination networks.

Thermal Analysis (TGA)

View Article Online
DOI: 10.1039/D6DT00722H

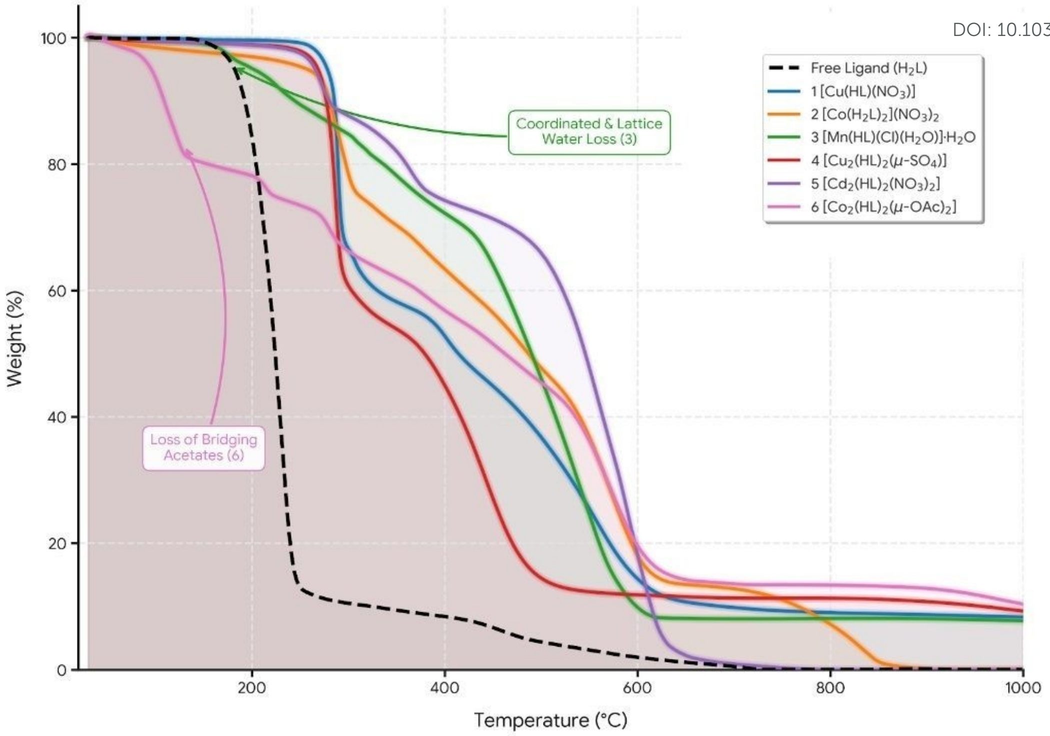

Figure 4. Cascading thermogravimetric analysis (TGA) profiles (the "Niagara" plot) of the free ligand (H_2L) and its corresponding complexes (**1**-**6**). The highly stable plateau regions demonstrate the pronounced thermal robustness imparted by the supersaturated multinuclear architectures. The distinct initial weight loss in the Mn(II) monomer (**3**) quantitatively aligns with the dehydration of its uncoordinated lattice water molecule (~4.9%), while the early decomposition step in the Co(II)-acetate dimer (**6**) signifies the breakdown of the sterically encumbered acetate bridging network.

The thermal robustness and specific decomposition pathways of the free ligand and the supramolecular architectures (**1**–**6**) were evaluated via thermogravimetric analysis (TGA) from ambient temperature up to 1000 ˚C under a nitrogen atmosphere. As depicted in the cascading thermal profiles (**Figure 4**), the free ligand exhibits a relatively low thermal decomposition threshold, rapidly losing its mass beyond 200 ˚C. In stark contrast, the TGA profiles of complexes **1**–**6** demonstrate a remarkable enhancement in thermal stability upon metal coordination.[22] This outstanding thermal robustness is a direct macroscopic consequence of the highly cross-linked, rigid dimeric and polymeric architectures stabilized by the robust μ-phenoxo and μ-anion bridges.[23] Initial minor weight losses below 150 ˚C for some complexes correspond to the removal of lattice solvent molecules.

View Article Online
DOI: 10.1039/D6DT00722H

A detailed examination of the TGA profile for the mononuclear Mn(II) complex (**3**) reveals a characteristic two-step weight loss before the main framework decomposition. The initial minor weight loss of ~1.0% below 130 ˚C is attributed to the release of non-coordinated lattice water molecules, which are loosely held within the crystal voids via hydrogen-bonding networks. This is immediately followed by a more pronounced weight loss step between 140 ˚C and 200 ˚C (totaling ~4.9% for both steps), which perfectly corresponds to the calculated value (4.87%) for the elimination of one coordinated water molecule. This stepwise thermal behavior provides strong macroscopic evidence for the distinct environments (hydrogen-bonded vs. metal-coordinated) of the water molecules in the Mn(II) architecture.[24] For all complexes, the major frameworks undergo complete thermal degradation above 400–500 ˚C to yield the respective metal oxides as final residues.

Furthermore, the terminal decomposition phases observed in the TGA curves (up to ~1000 ˚C) provide robust quantitative verification of the bulk metal stoichiometry. The final residual plateaus for the majority of the complexes (yielding experimental residual masses ranging from ~7.8% to 10.7%) are in excellent agreement with the theoretically calculated mass percentages for their respective terminal metal oxides (e.g., CuO, CoO, and MnO).[25,26] Conversely, for specific coordination spheres (such as the Cd(II) complex), the nearly complete mass loss observed at these extreme temperatures is physically consistent with the well-documented high-temperature sublimation of their resultant metal oxides (e.g., CdO).[27,28] This quantitative agreement between the experimental thermal residues and the theoretical oxide masses conclusively validates the structural composition of the synthesized networks.

Morphological Diversity and Hierarchical Self-Assembly

View Article Online
DOI: 10.1039/D6DT00722H

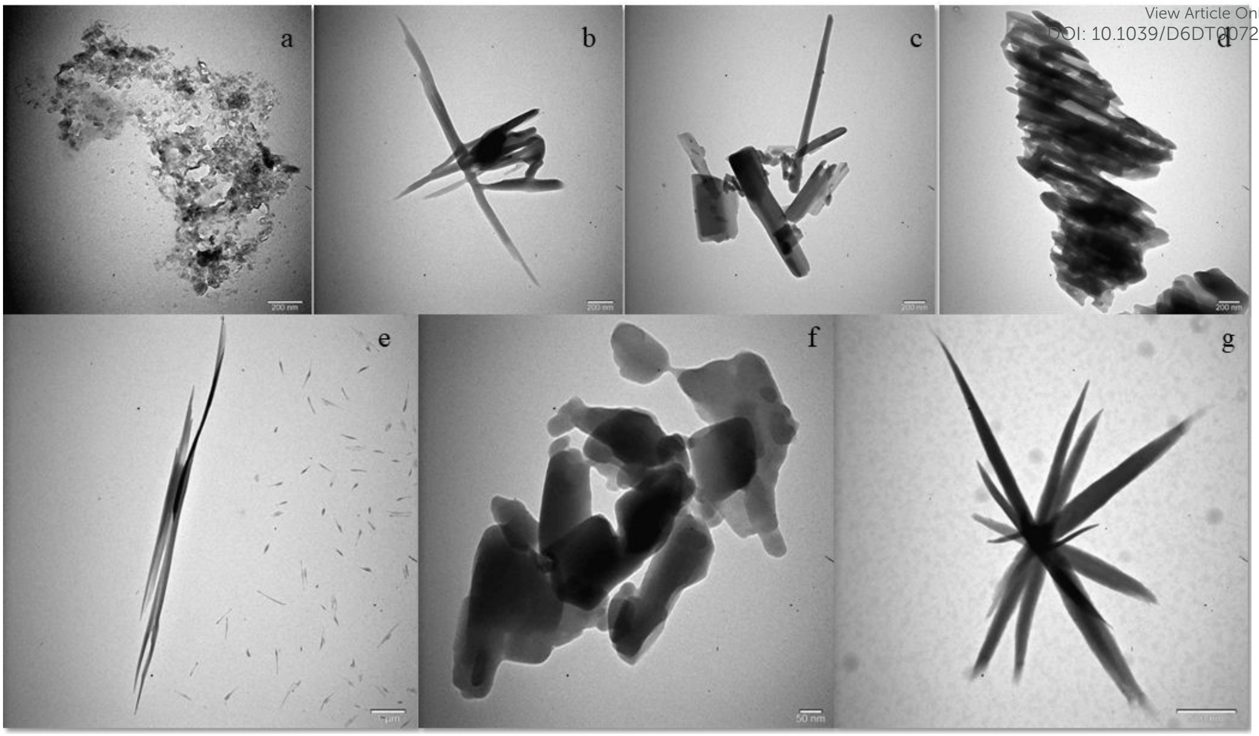

Figure 5. Transmission electron microscopy (TEM) images showing the morphological evolution of the synthesized compounds: (**a**) the free ligand, and (**b–g**) complexes **1–6**, respectively. **Scale bars: (a) 200 nm, (b) 200 nm, (c) 200 nm, (d) 200 nm, (e) 1 μm, (f) 50 nm, (g) 500 nm.**

The profound influence of counter-anion exchange on the hierarchical self-assembly of these nodes is unequivocally demonstrated by transmission electron microscopy.[29] The profound influence of the coordination geometry on the nanoscale self-assembly was unequivocally demonstrated by transmission electron microscopy (TEM) (**Figure 5**). A spectacular morphological evolution, entirely dictated by the central metal and extreme stoichiometry, was observed. The pure organic free ligand exhibited severe electron-beam-induced damage, appearing as an amorphous mass (**Figure 5a**). In stark contrast, the metal complexes displayed highly ordered and distinct architectures. Notably, the perfect octahedral symmetry (with trans angles approaching ~179.58°) of the mononuclear Co(II) complex (**2**) facilitated the growth of regular, highly ordered 1D nanorods.[30] However, the pronounced Jahn-Teller distortion in the mononuclear Cu(II) complex (**1**) strictly confined the anisotropic growth, yielding exceptionally uniform and ultra-thin 1D nanowires with an average diameter of ~5 nm. As

View Article Online
DOI: 10.1039/D6DT00722H

expected, transitioning to dinuclear and polymeric systems dramatically altered the topologies. The bromide-bridged polymeric network of Cd(II) complex (**5**) restricted 1D extension, instead driving the formation of massive, heavily fused continuous aggregates composed of sub-50 nm primary particles. Meanwhile, the dinuclear Cu(II) complex (**4**) exhibited pronounced morphological polymorphism, featuring both continuous networks and >100 nm thick fibers. Finally, complexes **3** and **6** formed massive, irregular aggregates characterized by sponge-like interstitial cavities, likely resulting from rapid, defect-rich agglomeration. This remarkable morphological diversity underlines how atomic-level crystallographic variations translate into profound macroscopic structural differences.[31]

Computational Studies: Molecular Electrostatic Potential (MEP) Analysis

To gain a deeper understanding of the structure-reactivity relationship and the electronic driving forces behind the supramolecular assembly, Molecular Electrostatic Potential (MEP) maps were computed.[32] The MEP surface of the uncoordinated free ligand (**Figure 6A**) serves as a crucial baseline. It exhibits highly intense negative electrostatic regions (depicted in red, indicating strongly nucleophilic zones) strictly localized over the phenolic and alcoholic oxygen atoms. These electron-rich pockets act as pre-organized Lewis base 'hotspots', mathematically dictating the specific coordination sites. Strikingly, even in the uncoordinated state, the outermost tips of the peripheral bromine atoms exhibit a distinct electropositive character (blue regions). This confirms that the structure-directing σ-hole effect is an inherent feature of the rationally designed halogenated scaffold.

View Article Online
DOI: 10.1039/D6DT00722H

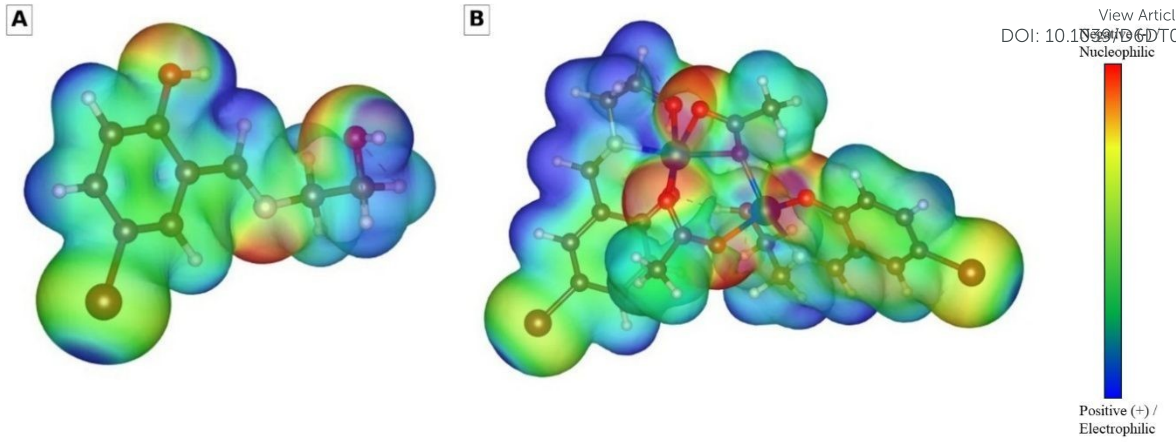

Figure 6. Comparative Molecular Electrostatic Potential (MEP) surfaces mapped onto the electron density distributions, illustrating the profound charge redistribution upon complexation. **(A)** The free ligand (H_2L), highlighting the nucleophilic regions (red) localized on the heteroatoms and the characteristic electrophilic σ-hole (blue/green) on the terminal bromine atom. **(B)** The highly constrained binuclear Co(II)-acetate dimer (**6**), revealing a dramatic electrostatic polarization. The immense concentration of electron density around the bridging core (deep red) starkly contrasts with the electrophilic periphery. This massive electronic imbalance and resulting dipole moment serve as the primary driving forces dictating the hierarchical self-assembly, ultimately triggering the formation of the macroscopic 3D starfish-like architectures. The accompanying color scale illustrates the electrostatic potential trend, ranging from negative (nucleophilic) regions in red to positive (electrophilic) regions in blue, with the local surface potentials mapped in kcal/mol.

Upon metal complexation across the synthesized series, a dramatic redistribution of electron density is observed. The intense red regions over the bridging oxygens significantly diminish, shifting toward neutral or slightly positive potentials. This 'electronic quenching' visually confirms the successful donation of electron density from the oxygen lone pairs to the metal *d*-orbitals, validating the strong covalent nature of the coordination networks. Despite these drastic coordination-induced topological changes, the electropositive σ-holes on the terminal bromine atoms remain robustly conserved across all complexes.[33] This universally persistent halogen-based anisotropy acts as a reliable supramolecular anchor dictating the ultimate solid-state packing.[34]

Most importantly, the comparative MEP analysis provides profound theoretical insights into the hierarchical morphological evolution observed via TEM (**Figure 5**). For the mononuclear

Co(II) complex (**2**), the MEP surface reveals a highly polarized protonated coordination sphere, rendering the terminal protons exceptionally potent hydrogen-bond donors. This highly directional polarization strictly drives the 0D building blocks into uniform 1D nanorods (1621 nm) via charge-assisted hydrogen bonds with outer-sphere nitrates. Conversely, the discrete binuclear Co(II)-acetate dimer (**6**) exhibits a sharply polarized charge distribution across its core (**Figure 6B**). The immense concentration of electron density around the bridging acetate and phenoxo moieties establishes potent electrostatic binding sites, which starkly contrast with the electrophilic periphery. This massive internal electrostatic dichotomy effectively transforms the dimer into a highly directional supramolecular synthon.[35] The resulting robust dipole-dipole interactions act as the primary electrostatic 'glue', orchestrating the spontaneous head-to-tail stacking of the dimers and their ultimate hierarchical evolution into the complex 3D starfish-like architectures (~5000 nm).

Table 3. Comprehensive summary of the core theoretical findings, including Frontier Molecular Orbital (FMO) energies and Molecular Electrostatic Potential (MEP) extremes for the free ligand and synthesized complexes.

Compound	**Spin State**	**E_{HOMO}(eV)**	**E_{LUMO}(eV)**	**ΔE (eV)**	**Global $V_{s,min}$ (kcal/mol)**	**Global $V_{s,max}$ (kcal/mol)**	**Halogen σ-hole $V_{s,max}$ (kcal/mol)**
Free Ligand	Closed-shell	-6.04	-1.51	4.53	-26.69	+47.07	+7.50
1	α-spin	-6.08	-2.35	3.73	-28.93	+39.14	+13.27
	β-spin	-6.03	-3.63	2.40			
2	α-spin	-11.77	-8.16	3.61	+79.26	+191.39	+100.80
	β-spin	-11.77	-8.87	2.90			
3	α-spin	-5.78	-1.99	3.78	-35.17	+52.91	+11.15
	β-spin	-5.97	-2.08	3.89			

4	α-spin	-5.77	-2.40	3.37	-43.40	+35.81	+9.88; +14.83
	β-spin	-5.73	-3.72	02.01			
5	Closed-shell	-6.14	-2.36	3.78	-39.92	+44.58	+12.31; +12.01
6	α-spin	-5.34	-1.97	3.37	-31.70	+42.53	+5.04; +10.81
	β-spin	-5.39	-2.09	3.30			

As summarized in **Table 3**, the coordination of the metal centers induces a profound polarization across the ligand framework, drastically altering the electrostatic landscape. Specifically, the electropositive σ-hole strictly localized on the halogen atom along the C–Br bond axis deepens significantly upon complexation. For instance, while the free ligand exhibits a modest σ-hole potential of $V_{s,max}$ = +7.50 kcal/mol, this value nearly doubles in the flagship complex **1** (+13.27 kcal/mol). This metal-induced enhancement transforms the halogen into a highly activated electrostatic receptor, perfectly pre-organizing the supramolecular network for the robust and highly directional Br···O halogen bonds quantified via the subsequent QTAIM and NCI analyses. Taking this a step further, the extreme case of the cationic Co(II) monomer (2) demonstrates a highly positive absolute σ-hole potential of +100.80 kcal/mol. It is important to note that this exceptionally high absolute value simply originates from the net positive charge of the overall complex, which uniformly shifts the entire electrostatic potential baseline to higher positive values (as evidenced by a global $V_{s,min}$ of +79.26 kcal/mol). When this physical baseline shift is accounted for, the relative depth of the σ-hole compared to its immediate surroundings is approximately ~21 kcal/mol, remaining completely consistent with classical halogen bonding characteristics.[36, 37]

View Article Online
DOI: 10.1039/D6DT00722H

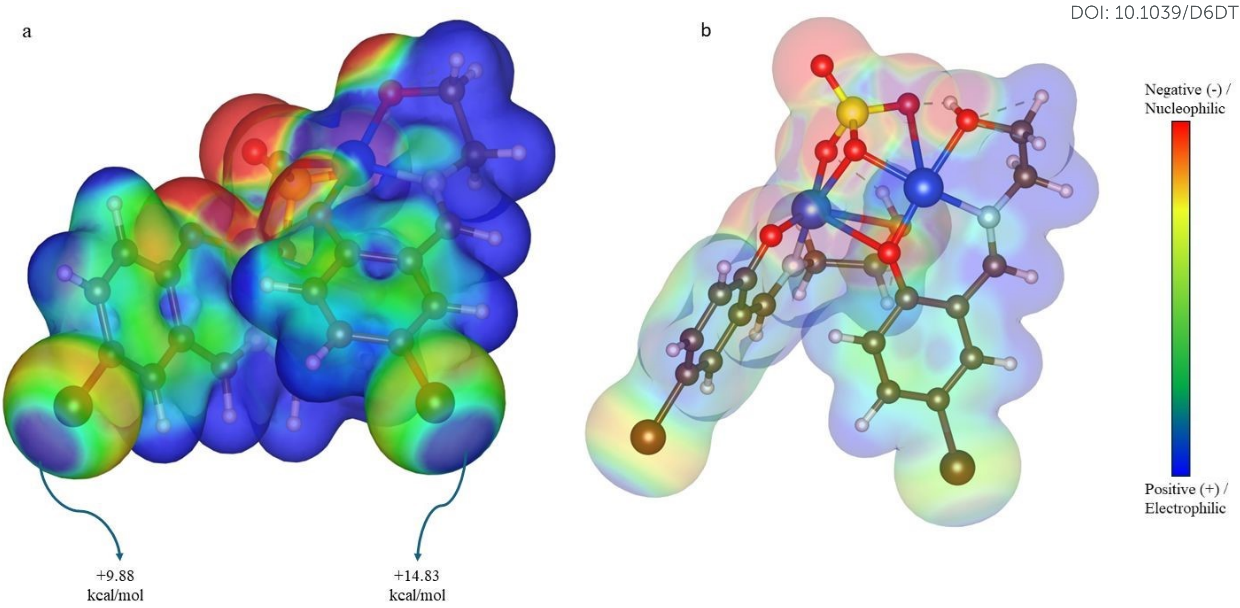

Figure 7. 3D spatial electron density distributions rendered via VESTA, physically visualizing the divergent halogen bonding donor capacities of the two crystallographically independent bromine atoms in the asymmetric binuclear Cu(II)-sulfate complex (**4**). **(a)** Opaque view showcasing the specific halogen σ-hole potentials. The distinct isosurface topologies and local electron density maxima (indicated by arrows at the nuclear positions) provide a direct visual rationale for their contrasting σ-hole potentials (+9.88 kcal/mol vs. the highly activated +14.83 kcal/mol). **(b)** Semitransparent view revealing the underlying coordination sphere. This projection explicitly demonstrates how the classic Jahn-Teller distortion of the d^9 Cu(II) center, which destabilizes the 6-coordinate side via axial elongation, reduces metal-ligand orbital overlap and inherently modulates the polarization capacity of each corresponding halogen atom. The accompanying color scale illustrates the electrostatic potential trend, ranging from negative (nucleophilic) regions in red to positive (electrophilic) regions in blue, with the local surface potentials mapped in kcal/mol.

Interestingly, the magnitude of the σ-hole is profoundly dictated by the interplay between the metal's electronic configuration (e.g., Jahn-Teller effects) and its preferred coordination geometry, rather than the coordination number alone. In the asymmetric binuclear Cu(II)-sulfate complex (**4**), the 5-coordinate metal center induces a significantly larger σ-hole (+14.83 kcal/mol) compared to its 6-coordinate counterpart (+9.88 kcal/mol). This reversal is a classic manifestation of the Jahn-Teller distortion inherent to d^9 Cu(II) ions, which destabilizes the 6-coordinate geometry via axial elongation, thereby weakening the metal-ligand orbital overlap and reducing its electron-withdrawing capacity **(Figure 7)**. Conversely, in the Co(II)-acetate

View Article Online
DOI: 10.1039/D6DT00722H

complex (**6**), the d^7 metal center inherently favors a 6-coordinate octahedral environment. Supported by flexible acetate ligands, the 6-coordinate Co(II) achieves optimal orbital overlap, making it the stronger electron-withdrawing center and generating a larger σ-hole (+10.81 kcal/mol) than the 5-coordinate side (+5.04 kcal/mol). This delicate balance highlights how specific metal-ion preferences modulate the halogen bond donor capacity across the supramolecular network.[38]

Topological and Non-Covalent Interaction (NCI) Analysis of the Supramolecular Anchor

Among the synthesized series, the mononuclear Cu(II) complex (**1**) exhibits the most extreme structural anomaly, characterized by an unusually short Br···O contact (2.71 Å). Therefore, it was selected as the flagship model for an in-depth quantum topological investigation to unearth the thermodynamic driving forces dictated by the extreme metal-to-ligand ratio.[39]

To elucidate the underlying thermodynamic driving forces that dictate the coordination topology, the nature of this short Br···O contact was quantitatively investigated using Density Functional Theory (DFT) alongside Quantum Theory of Atoms in Molecules (QTAIM) and Non-Covalent Interaction (NCI) analyses. The NCI analysis, based on the reduced density gradient (RDG), revealed a highly localized, green disc-shaped isosurface between the bromine and the coordinated nitrate oxygen atoms. (**Figure 8a-8b**). The corresponding 2D scatter plot exhibited a sharp spike in the negative region at $\mathrm{sign}(\lambda_2)\rho \approx -0.025$ a.u., visually and mathematically confirming the presence of a strongly attractive, highly directional halogen bond rather than a weak van der Waals dispersion (**Figure 8c**). Alongside this primary interaction, adjacent smaller isosurface discs indicate the presence of secondary C-H···O weak

View Article Online
DOI: 10.1039/D6DT00722H

hydrogen bonds, which act cooperatively with the primary halogen bond to rigidly lock the conformation.[40]

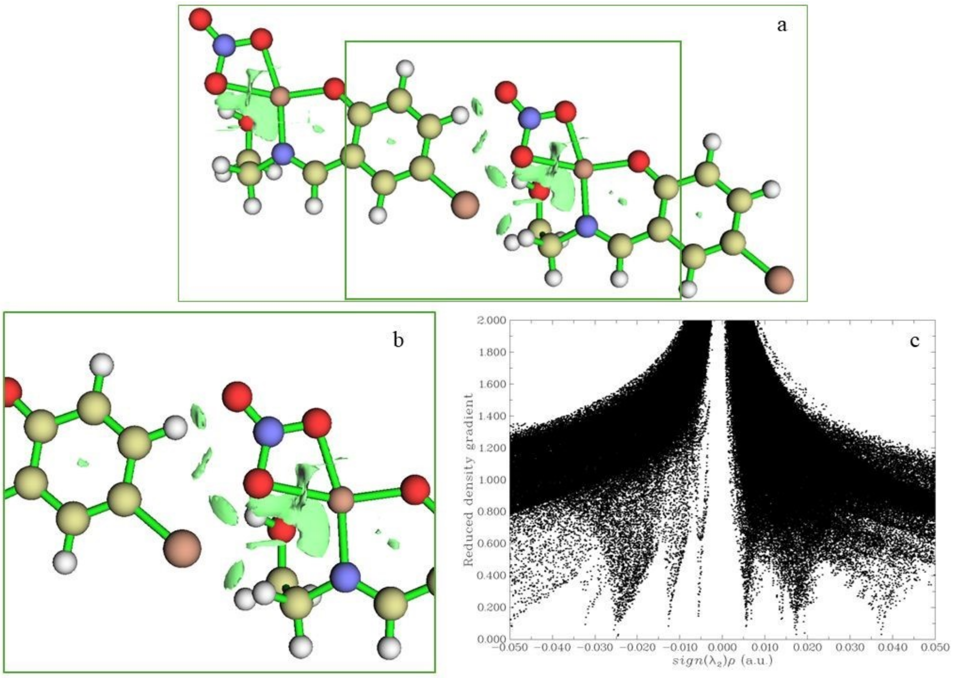

Figure 8. Multi-modal quantum topological investigation of the structure-directing halogen bond in the flagship complex (**1**). **(a)** Full 3D NCI isosurface map. A green rectangle inset explicitly delineates the inter-molecular Br···O contact region. **(b)** Magnified view of the inset in (a), showcasing a detailed close-up of the highly localized, attractive green disc. This cropped visualization distinctly demonstrates the powerful and directional supramolecular anchor coercing the extreme coordination topology. **(c)** High-resolution 2D RDG vs. sign(λ_2)ρ scatter plot, with the prominent spike at sign(λ_2)$\rho \approx -0.025$ a.u. quantitatively defining the powerful, non-dispersive Br···O halogen bond, clearly separated from weak van der Waals interactions.

To quantify the strength of this supramolecular anchor, QTAIM topological analysis was performed following Bader's formalism. A distinct bond critical point (BCP) was located along the Br···O bond path. The electron density at the BCP (ρ) was calculated as 0.0255 a.u., falling well within the accepted upper range for strong non-covalent interactions. The positive value of the Laplacian of the electron density ($\nabla^2\rho$ = +0.1009 a.u.) explicitly characterized the contact as a closed-shell interaction. Most importantly, utilizing the local potential energy density (V(r)=-0.01991 a.u.) at the BCP, the interaction energy (E_{int}) was calculated as ~6.25

View Article Online
DOI: 10.1039/D6DT00722H

kcal/mol. Such a substantial binding energy firmly establishes this halogen bond not merely as a packing artifact, but as a structure-directing thermodynamic anchor that coerces the system into its unique coordination topology, effectively overriding the classical steric and electronic expectations of extreme metal-to-ligand ratios.

To precisely contextualize the strength and physical nature of these non-covalent interactions, the calculated QTAIM parameters were compared with structurally similar halogenated Schiff base complexes reported in the literature.[41] According to established topological criteria, standard non-covalent interactions (such as halogen and hydrogen bonds) exhibit electron density ($\rho(r)$) values at the bond critical point (BCP) ranging from 0.002 to 0.035 a.u., accompanied by a positive Laplacian $\nabla^2\rho(r) > 0$), which is indicative of classical closed-shell electrostatic interactions.[42] In the present kinetically trapped architectures, the calculated ($\rho(r)$ and $\nabla^2\rho(r)$ values for the crucial Br···O halogen bonds and the accompanying hydrogen bonds perfectly align with these established literature benchmarks. Furthermore, the ratio of kinetic to potential energy densities ($-G(r)/V(r) > 1$) unequivocally categorizes these supramolecular anchors as purely non-covalent. This comparative topological analysis conclusively validates that despite the extreme 10:1 supersaturation and severe coordination stress, the supramolecular synthons driving the 3D assembly exhibit thermodynamic and electronic characteristics highly consistent with classically synthesized systems.[43]

Computational Studies: Frontier Molecular Orbital (FMO) and Spin Density Analysis

View Article Online
DOI: 10.1039/D6DT00722H

The calculated HOMO and LUMO energies, along with their corresponding ΔE gaps, are summarized in **Table 3**. A dramatic narrowing of the energy gap is observed upon metal coordination, particularly for the β-spin states of the paramagnetic derivatives, underscoring the electronic influence of the metal centers on the ligand framework.

To establish a definitive electronic baseline, the Frontier Molecular Orbital (FMO) energies and spatial topographies of the rationally designed free ligand were evaluated (**Figure 9**). The uncoordinated scaffold reveals a profoundly wide HOMO–LUMO gap of 4.53 eV, reflecting its high intrinsic chemical hardness and kinetic stability. Upon complexation, the integration of metallic *d*-orbitals inherently stabilizes the LUMO levels, consistently narrowing the energy gap across the synthesized series (e.g., to 3.78 eV in the Cd(II) dimer and 2.01–3.36 eV in the open-shell analogues). Despite this expected complexation-induced reduction, the fundamental energy gaps remain robustly large. According to Pearson's maximum hardness principle, these substantial energy barriers dictate a high degree of kinetic inertness.[44] This theoretically determined electronic rigidity acts as the quantum mechanical origin of the outstanding macroscopic thermal resilience (resisting decomposition up to 400–500 ˚C) observed in the TGA profiles.

View Article Online
DOI: 10.1039/D6DT00722H

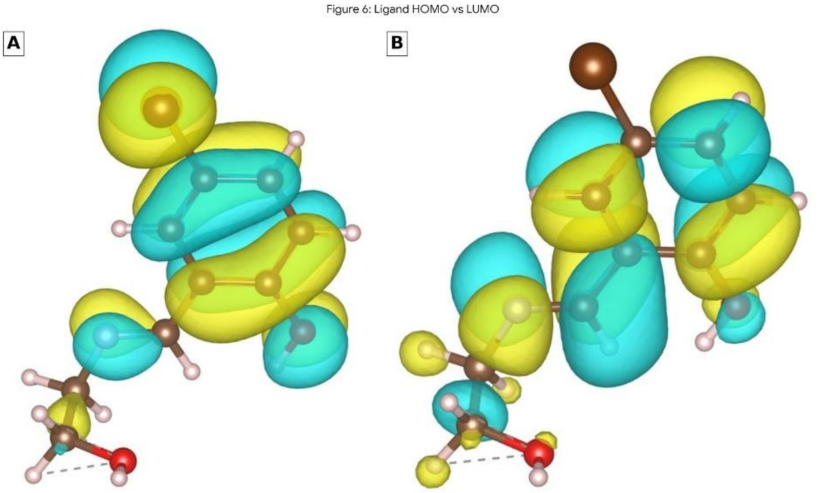

Figure 9. Frontier Molecular Orbital (FMO) topography of the uncoordinated free ligand (H_2L). **(a)** The HOMO is predominantly localized over the extended π-conjugated system and phenoxo moiety, establishing potent electron-donor 'hotspots'. **(b)** The LUMO exhibits characteristic π -antibonding nodal planes, completely vacating the aliphatic and terminal halogen segments, thereby regioselectively priming the scaffold for transition metal capture.

Beyond energetic stability, the spatial topography of the FMOs elegantly captures the crystallographic asymmetry inherent to the multinuclear architectures, notably transforming them into intrinsic "Asymmetric Charge Transfer".[45] For instance, as vividly captured in the FMO maps of the discrete Co (II)-acetate dimer (**6**), the distinct primary coordination spheres drive an extraordinary spatial symmetry breaking (**Figure 10**). The HOMO electron density acts as a localized electron donor strictly confined to one half of the asymmetric dimer, while the LUMO is profoundly segregated onto the opposite metallic core and its coordinating ligand. This spectacular spatial polarization establishes highly directional Ligand-to-Ligand (LLCT) and Metal-to-Metal Charge Transfer (MMCT) pathways, demonstrating how subtle geometric variations dictate the electronic reactivity of the entire supramolecular architecture.

View Article Online
DOI: 10.1039/D6DT00722H

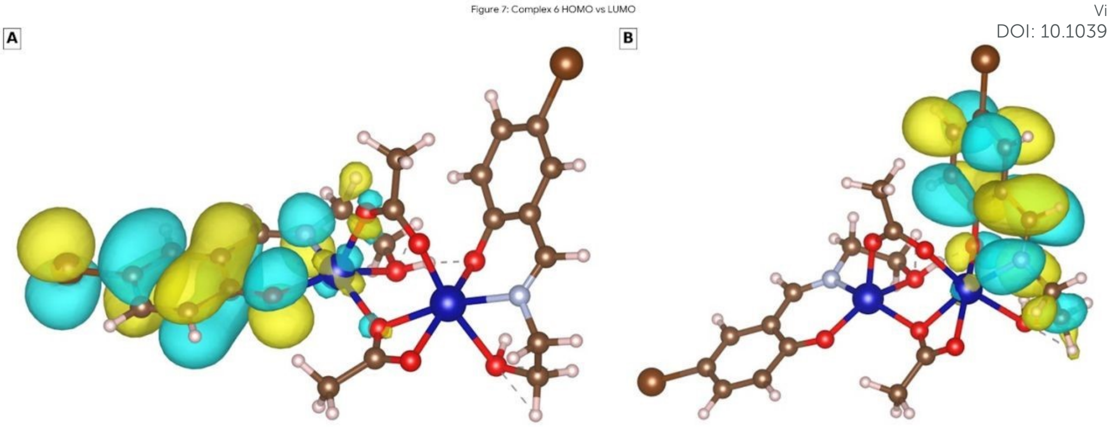

Figure 10. Spatial distribution of the α-spin Frontier Molecular Orbitals for the asymmetric binuclear Co(II)-acetate dimer (**6**). The profound spatial segregation of the **(A)** HOMO and **(B)** LUMO onto opposite halves of the dimeric core vividly visualizes a massive symmetry breaking. This "molecular diode" topology dictates highly directional intramolecular charge transfer (LLCT) pathways, driven by the distinct primary coordination spheres of the metal centers.

For the open-shell paramagnetic complexes (**1**, **2**, and **3**), unrestricted DFT calculations reveal significant spin polarization, where the global fundamental gaps are dictated by the stabilized β-spin manifolds. The 3D spin density topological analyses vividly map the unpaired electron distributions (**Figure 11**), such as the archetypal $d_{x^2-y^2}$ target orbital geometry in the highly Jahn-Teller distorted Cu (II) center (**1**) and the massive spherical magnetic lobe of the high-spin d^5 Mn (II) core (**3**). Crucially, pronounced spin delocalization is consistently observed over the directly coordinating heteroatoms (the ligand's donor 'teeth') across the series. This distinct spin leakage into the ligand's *p*-orbitals provides direct theoretical evidence of substantial orbital mixing, unequivocally confirming the strong covalent character of the primary coordination bonds that stabilize these isolated magnetic nodes.[46]

View Article Online
DOI: 10.1039/D6DT00722H

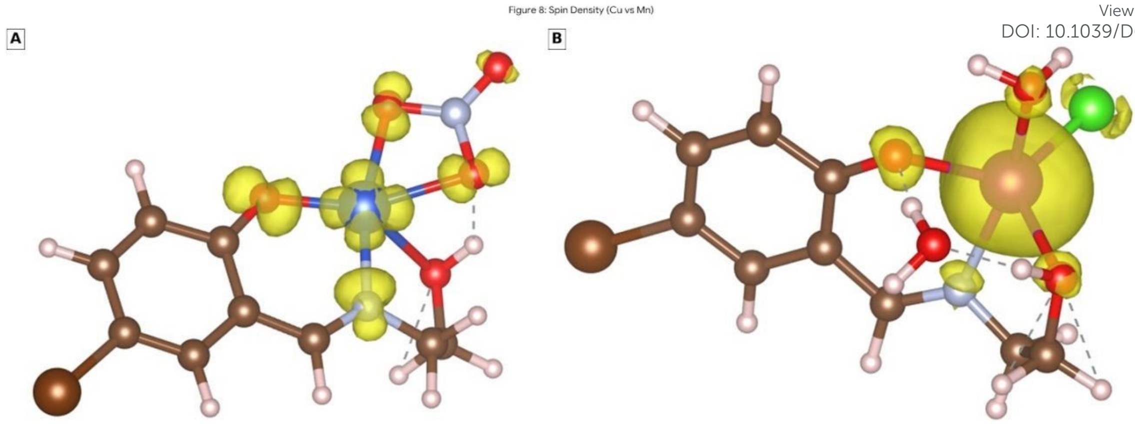

Figure 11. 3D Spin Density maps (isosurface value = 0.002 a.u.) illustrating the unpaired electron distribution in the open-shell complexes. **(A)** The strongly Jahn-Teller distorted Cu(II) complex (1), revealing the characteristic $d_{x^2-y^2}$ magnetic lobe. **(B)** The high-spin d^5 Mn(II) complex (3). Both topographies demonstrate distinct spin delocalization (leakage) onto the coordinating heteroatoms, theoretically confirming the robust covalent character of the metal-ligand primary coordination bonds.

Conclusions

In conclusion, subjecting a flexible Schiff base ligand to a supersaturated "metal salt sea" (via an extreme 10:1 metal-to-ligand stoichiometry) has been demonstrated as a powerful synthetic strategy to access unprecedented, anion-directed structural diversity. The structural elucidation of these kinetically trapped microcrystalline powders, achieved through a rigorous *ab initio* Powder X-ray Diffraction (PXRD) approach, revealed a striking structural transition from discrete monomeric species to robust highly-bridged binuclear architectures.[47, 48]

Comprehensive DFT calculations and MEP mapping provided profound insights into the driving forces behind this assembly, identifying a universally conserved σ-hole at the peripheral bromine atoms as the primary supramolecular anchor across all complexes. Importantly, these quantum chemical investigations extended beyond structural parameters to unveil the intricate electronic and magnetic architecture of the materials. FMO and 3D spin density analyses elucidated highly directional charge transfer channels (LMCT/LLCT) and

View Article Online
DOI: 10.1039/D6DT00722H

unmasked robust superexchange pathways, visually confirming the strong covalent character within the primary coordination spheres. The identification of symmetry-breaking "Asymmetric Charge Transfer" with tunable energy gaps ($\Delta E = 2.01–3.89$ eV) and anisotropic magnetic topologies—ranging from isolated 0D magnetic nodes to highly coupled networks—highlights the immense potential of these materials in advanced molecular electronics.

Beyond electronic properties, the structural elucidations underscore the profound impact of competitive counter-anion coordination on the resulting topologies. The immense steric constraints within the binuclear frameworks drive extreme geometric deformations, stabilizing rare coordination environments, such as a highly distorted intermediate trapped along the Bailar twist pathway ($O_h \rightarrow D_{3h}$) and a strictly validated square-pyramidal geometric distortion ($\tau = 0.303$). Ultimately, these fundamental sub-nanometer topological features seamlessly orchestrate the remarkable macroscopic morphological evolution observed via TEM. The structure-directing power of the extreme metal stoichiometry completely dictates the nanoscale growth regime. This evolution transitions from the electron-beam-induced amorphous state of the pure organic ligand to highly ordered 1D architectures, such as the ultra-thin (~5 nm) nanowires of the Jahn-Teller distorted Cu(II) monomer and the uniform nanorods of the perfectly octahedral Co(II) complex. Consequently, transitioning to dinuclear and polymeric systems completely disrupts isolated 1D growth, driving the formation of polymorphic networks, heavily fused sub-50 nm polymeric clusters, and massive sponge-like aggregates with interstitial cavities.

Significantly, this study demonstrates that extreme metal-to-ligand stoichiometries do not merely result in random kinetic precipitations, but are governed by powerful, structure-directing non-covalent forces. Advanced quantum topological analyses (QTAIM and NCI) of the flagship mononuclear complex explicitly quantified a robust and highly directional Br···O halogen bond. With a remarkably high stabilization energy of ~6.25 kcal/mol, this supramolecular anchor coercively dictates the ultimate coordination topology, effectively overriding classical steric expectations. Ultimately, navigating the 'metal salt sea' requires a fundamental understanding of these thermodynamic anchors, paving the way for the rational design of novel halogenated coordination architectures.

Finally, the thermodynamic robustness of these intricate networks was macroscopically validated through Thermogravimetric Analysis (TGA), exhibiting outstanding thermal stability up to 400–500 ˚C. The flawless synergy between empirical physicochemical characterizations, theoretical electrostatic simulations, and robust direct-space structural models establishes extreme concentration gradients as a highly effective tool in predictive crystal engineering and the rational design of hierarchical functional materials.

Based on these robust findings, the future research roadmap for these kinetically trapped complexes is explicitly directed toward their application in advanced molecular electronics and solid-state device engineering. The unique combination of structural asymmetry, tunable semiconductor-like energy gaps ($\Delta E \approx 2.0$–3.8 eV), highly directional charge transfer channels, and outstanding thermal stability (up to 500 ˚C) positions these supramolecular networks as highly promising candidates for molecular spintronics and high-temperature sensor arrays.

Moving forward, my future research will focus on synthesizing similar and diverse series of complexes using various ligand scaffolds and metal centers to further map the chemical space of the 'metal salt sea' and validate the universality of this kinetic trapping strategy. Consequently, these materials offer a robust platform for future interdisciplinary studies aimed at fabricating thin-film devices from these bulk powders, enabling the broader materials science community to empirically evaluate their electronic switching and "Asymmetric Charge Transfer" capabilities under practical operating conditions.

Methodology

Materials and Physical Measurements

All reagents and metal salts ($Cu(NO_3)_2{\cdot}3H_2O$, $Co(NO_3)_2{\cdot}6H_2O$, $MnCl_2{\cdot}4H_2O$, $CuSO_4{\cdot}5H_2O$, $Cd(NO_3)_2{\cdot}4H_2O$, and $Co(CH_3COO)_2{\cdot}4H_2O$) were purchased from commercial sources and used without further purification. Elemental analyses for the ligand and complexes were carried out using standard methods with a Eurovector 3018 CHNS analyzer. Fourier-transform infrared (FT-IR) spectra were recorded on a PerkinElmer 65 spectrometer in the range of 4000–400 cm^{-1}. Thermogravimetric analyses (TGA) were carried out using a Perkin Elmer TGA 8000 thermal analyzer under a nitrogen atmosphere with a heating rate of 10 ˚C/min from ambient temperature up to 1000 ˚C. The nanoscale morphological features of the synthesized coordination polymers were investigated utilizing Transmission Electron Microscopy (TEM) on a JEOL JEM-1400 PLUS instrument operating at 80 kV.

Powder X-ray diffraction (PXRD) data were collected on a Panalytical Empyrean diffractometer equipped with a Cu Kα radiation source (λ_1 = 1.54056 Å, λ_2 = 1.54439 Å) operating at 45 kV and 40 mA. The diffraction patterns were recorded at room temperature over a 2θ range of 5.00˚ to 60.00˚ or 65.00˚ with a step size of approximately 0.013˚. The structural solution and subsequent Rietveld refinement procedures were carried out using the EXPO2014 software package, utilizing the simulated annealing algorithm.

General Synthesis of Complexes 1–6 (The "Supersaturated Metal Sea" Approach)

The Schiff base ligand (H_2L) was synthesized and purified from ethanolamine and 5-bromosalicylaldehyde according to a previously reported procedure.[49] To explore the structural diversity driven by extreme metal concentrations, a unique 10:1 (metal-to-ligand) stoichiometric ratio was employed for the synthesis of all complexes. In a typical procedure, the ethanolamine-based ligand (1.0 mmol) was completely dissolved in hot absolute ethanol (10 mL). To this solution, a highly concentrated solution of the respective metal salt (10.0 mmol), independently dissolved in hot absolute ethanol (10 mL), was added dropwise under continuous stirring. The resulting mixture was stirred under heating for 30 minutes to ensure complete complexation and to overcome any kinetic barriers impeding polynuclear assembly. The solution was then filtered while hot to remove any trace impurities and allowed to stand undisturbed at room temperature. Slow evaporation of the ethanol solvent over a period of several days yielded microcrystalline powders or single crystals suitable for X-ray diffraction analysis. The solid complexes were collected by filtration, washed with cold ethanol, and dried in air. As anticipated, the extreme 10:1 metal-to-ligand reaction regimes successfully yielded a diverse series of novel transition metal architectures.

View Article Online
DOI: 10.1039/D6DT00722H

It is important to note that the extreme 10:1 metal-to-ligand stoichiometry was not selected arbitrarily, but was determined as the optimal kinetic 'sweet spot' through preliminary synthetic screenings. Lower supersaturation ratios (e.g., 2:1 to 5:1) failed to provide the necessary coordination stress, predominantly yielding amorphous precipitates or thermodynamically stable, phase-impure mixtures. Conversely, excessively high ratios (e.g., 15:1 or 20:1) resulted in the severe co-precipitation of unreacted metal salts. Attempting to remove these massive salt impurities via extensive washing inevitably induced solvolysis, disrupting the fragile, kinetically trapped supramolecular networks. Consequently, the 10:1 ratio was identified as the unique stoichiometric threshold required to forcefully drive the counter-anions into the inner coordination sphere while successfully isolating phase-pure microcrystalline powders suitable for rigorous *ab initio* PXRD structural elucidation.[50, 51]

Free Ligand (H_2L) Yield: 67.1%. **Anal. Calcd for** $C_9H_{10}BrNO_2$: C, 44.29; H, 4.13; N, 5.74. **Found:** C, 43.86; H, 4.09; N, 5.63. **FT-IR** (ATR, ν_{max}, cm^{-1}): 3365 (br, m), 1645 (s), 1596 (w), 1494 (s), 1440 (m), 1357 (m), 1200 (vs), 1145 (s), 1056 (s), 1029 (m), 922 (m), 871 (s), 850 (vs), 730 (s), 667 (w).

Complex 1 [Cu(HL)(NO_3)] Yield: 78.3%. **Anal. Calcd for** $C_9H_9BrCuN_2O_5$: C, 29.32; H, 2.46; N, 7.60. **Found:** C, 29.45; H, 2.39; N, 7.66. **FT-IR** (ATR, ν_{max}, cm^{-1}): 1622 (vs), 1525 (m), 1458 (vs), 1416 (m), 1324 (s), 1209 (s), 1178 (s), 1042 (vs), 977 (m), 911 (s), 889 (m), 868 (vs), 769 (m), 753 (vs), 688 (s).

View Article Online
DOI: 10.1039/D6DT00722H

Complex 2 $[Co(H_2L)_2](NO_3)_2$ **Yield:** 91%. **Anal. Calcd for** $C_{18}H_{20}Br_2CoN_4O_{10}$: C, 32.21; H, 3.00; N, 8.35. **Found:** C, 32.15; H, 2.96; N, 8.41. **FT-IR** (ATR, ν_{max}, cm^{-1}): 3119 (br, w), 2855 (m), 1633 (vs), 1522 (m), 1441 (vs), 1412 (m), 1387 (m), 1305 (s), 1231 (m), 1209 (s), 1163 (s), 1086 (vs), 1050 (m), 868 (s), 750 (s).

Complex 3 $[Mn(HL)(Cl)(H_2O)]\cdot H_2O$ **Yield:** 85%. **Anal. Calcd for** $C_9H_{13}BrClMnNO_4$: C, 29.26; H, 3.55; N, 3.79. **Found:** C, 29.15; H, 3.51; N, 3.82. **FT-IR** (ATR, ν_{max}, cm^{-1}): 3268 (br, m), 3258 (br, m), 1618 (vs), 1533 (m), 1446 (s), 1301 (s), 1211 (s), 1186 (s), 1071 (s), 1056 (m), 872 (vs), 775 (vs), 746 (m).

Complex 4 $[Cu_2(HL)_2(\mu\text{-}SO_4)]$ **Yield:** 89%. **Anal. Calcd for** $C_{18}H_{18}Br_2Cu_2N_2O_8S$: C, 30.48; H, 2.56; N, 3.95. **Found:** C, 30.29; H, 3.02; N, 4.02. **FT-IR** (ATR, ν_{max}, cm^{-1}): 3269 (br, m), 1618 (vs), 1533 (s), 1438 (vs), 1418 (m), 1299 (vs), 1211 (vs), 1186 (s), 1072 (m), 1055 (s), 974 (m), 911 (m), 871 (vs), 774 (vs), 745 (m).

Complex 5 $[Cd_2(HL)_2(NO_3)_2]_n$ **Yield:** 72%. **Anal. Calcd for** $C_{18}H_{18}Br_2Cd_2N_4O_{10}$: C, 25.89; H, 2.17; N, 6.71. **Found:** C, 26.12; H, 2.12; N, 6.64. **FT-IR** (ATR, ν_{max}, cm^{-1}): 1627 (vs), 1512 (m), 1437 (s), 1409 (vs), 1389 (m), 1297 (s), 1208 (s), 1158 (s), 1044 (m), 983 (w), 940 (w), 882 (w), 854 (vs), 748 (vs), 702 (m).

Complex 6 $[Co_2(HL)_2(\mu\text{-}OAc)_2]$ **Yield:** 79%. **Anal. Calcd for** $C_{22}H_{24}Br_2Co_2N_2O_8$: C, 36.59; H, 3.35; N, 3.88. **Found:** C, 36.66; H, 3.28; N, 3.95. **FT-IR** (ATR, ν_{max}, cm^{-1}): 3391 (br,

View Article Online
DOI: 10.1039/D5DT00722H

m), 1648 (vs), 1587 (m), 1443 (vs), 1414 (m), 1310 (s), 1214 (s), 1170 (s), 1100 (m), 1016 (s), 930 (m), 863 (m), 748 (m), 607 (m), 578 (m).

In the structural formulations presented herein, the fully protonated, neutral Schiff base ligand (containing both the intact phenolic and aliphatic alcoholic protons) is denoted as H_2L. Its mono-deprotonated, monoanionic form (where only the highly acidic phenolic proton is lost while the aliphatic alcohol moiety remains protonated) is denoted as HL^-. This protonation state is consistently corroborated by crystallographic charge balance requirements, characteristic long axial metal-oxygen bond distances, and the extensive intermolecular hydrogen-bonding networks observed.

Detailed descriptions of the SDPD procedures, Rietveld refinement strategies, and all computational parameters, including complete software citations, are provided in the Electronic Supplementary Information (ESI).[52-65]

Conflicts of interest

The author declares no competing interests.

Data availability

The datasets generated and analyzed during the current study are available within the manuscript and its Electronic Supplementary Information (ESI) file. The crystallographic data for the synthesized complexes have been deposited at the Cambridge Crystallographic Data Centre (CCDC) under the accession numbers; 2534339, 2534340, 2534341, 2534343, 2535251, 2536167. Copies of these data can be obtained free of charge via www.ccdc.cam.ac.uk/data_request/cif. Additional raw computational data, including

View Article Online
DOI: 10.1039/D6DT00722H

optimized geometries, input coordinates, and topological analyses, are available from the corresponding author upon reasonable request.

Supplementary information

Electronic supplementary information (ESI) available: Additional PXRD Rietveld refinement profiles, complete energetic parameters for the DFT calculations, and optimized Cartesian coordinates.

Acknowledgments

This work was financially supported by the Scientific Research Projects Coordination Unit (BAP) of Balikesir University under Grant Number 2023/194. The author expresses his sincere gratitude to Prof. Dr. Elif Gungor for her valuable scientific insights and continuous support throughout this study. Special thanks are extended to the dedicated associate degree researchers of the Yardan Laboratory for their meticulous assistance during the experimental and synthetic procedures. Furthermore, the author gratefully acknowledges Canakkale Onsekiz Mart University Research Department (COBILTUM) for providing access to their advanced laboratory and instrumental facilities.

Corresponding Author

Alper Yardan, Department of Chemistry and Chemical Processing Technologies, Altinoluk Vocational School, Balikesir University, 10870, Edremit, Balikesir, Turkey; orcid.org/0000-0001-6916-831X; Email: alperyardan@gmail.com

References

1 R. Chakrabarty, P. S. Mukherjee and P. J. Stang, *Chem. Rev.*, 2011, **111**, 6810–6918.

2 J. Perez and L. Riera, *Chem. Soc. Rev.*, 2008, **37**, 2658–2667.

3 R. Custelcean, *Chem. Soc. Rev.*, 2014, **43**, 1813–1824.

4 M. Jiang, Y. Bian, L. Zou, T. Liu, Z. Ji, W. Ren, Z. Guo, Y. Cao, Y. Jiao and H. Pan, *ACS Chem. Biol.*, 2025, **20**, 2574–2583.

5 S. Hazra, D. Majumdar, D. Das, L. Barman, S. Roy and S. Dalai, *Dalton Trans.*, 2026, **55**, 1584–1624.

6 A. Yardan, C. Hopa, Y. Yahsi, A. Karahan, H. Kara and R. Kurtaran, *Spectrochim. Acta A Mol. Biomol. Spectrosc.*, 2015, **137**, 351–356.

7 A. Yardan, Y. Yahsi, H. Kara, A. Karahan, S. Durmus and R. Kurtaran, *Inorg. Chim. Acta*, 2014, **413**, 55–59.

8 A. Yardan, A. Karahan, N. Burcu Arslan, C. Hopa, M. Gokmen, C. Kazak and R. Kurtaran, *Synth. React. Inorg. Met.-Org. Nano-Met. Chem.*, 2015, **45**, 1224–1233.

9 G. Cavallo, P. Metrangolo, R. Milani, T. Pilati, A. Priimagi, G. Resnati and G. Terraneo, *Chem. Rev.*, 2016, **116**, 2478–2601.

10 P. Politzer, J. S. Murray and T. Clark, *Phys. Chem. Chem. Phys.*, 2010, **12**, 7748–7757..

11 P. Restorp and J. Jr. Rebek, *J. Am. Chem. Soc.*, 2008, **130**, 11850–11851.

12 D. Majumdar, J. E. Philip, S. Roy, B. Gassoumi and H. Ghalla, *BMC Chem.*, 2025, **19**, 227.

13 In *Infrared and Raman Spectra of Inorganic and Coordination Compounds*, John Wiley & Sons, Ltd, 2008, pp. 149–354.

14 G. B. Deacon and R. J. Phillips, *Coord. Chem. Rev.*, 1980, **33**, 227–250.

15 W. I. F. David, K. Shankland, L. B. McCusker and C. Bärlocher, Eds., *Structure Determination from Powder Diffraction Data*, Oxford University Press, 2006.

16 B. J. Hathaway and D. E. Billing, *Coord. Chem. Rev.*, 1970, **5**, 143–207.

17 K. M. Anderson and J. W. Steed, *CrystEngComm*, 2007, **9**, 328–330.

18 S. Alvarez, P. Alemany, D. Casanova, J. Cirera, M. Llunell and D. Avnir, *Coord. Chem. Rev.*, 2005, **249**, 1693–1708.

19 A. Atakol, H. Nazir, I. Svoboda, M. L. Aksu and O. Atakol, *J Therm Anal Calorim*, 2020, **139**, 1863–1882.

20 D. Majumdar, A. Chatterjee, M. Feizi-Dehnayebi, N. S. Kiran, B. Tuzun and D. Mishra, *Heliyon*, 2024, **10**, e35591.

21 E. F. Belogolova, G. Liu, E. P. Doronina, S. M. Ciborowski, V. F. Sidorkin and K. H. Bowen, *J. Phys. Chem. Lett.*, 2018, **9**, 1284–1289.

22. C. Janiak, *Dalton Trans.*, 2003, 2781–2804.

View Article Online
DOI: 10.1039/D5DT00722H

23 S. Öz, P. A. Bozkurt, Ş. B. Sopacı, N. Acar and O. Atakol, *J. Nat. Appl. Sci.*, 2022, **26**, 200–210.

24 J. M. Moreira, R. Rodrigues, M. A. G. Trindade, K. C. dos Santos, M. M. da Silva, B. Tirloni, C. A. Brandl, G. C. Paveglio, D. Roman and C. T. de Carvalho, *Inorg. Chim. Acta*, 2025, **575**, 122443.

25 J. N. Kuate, M. Kuate, A. G. Paboudam, A. P. Yepseu, V. Circu, S. N. Dhuri and P. T. Ndifon, *J. Fluoresc.*, 2025, **35**, 11593–11603.

26 1T. F. Mitu, S. Islam, S. Akther, A. H. M. S. I. M. Jamal, S. P. Moulick, M. N. Uddin, M. A. A. Shaikh and P. K. Bakshi, *Appl. Organomet. Chem.*, 2025, **39**, e70203.

27 F. M. Ibrahim, *Indones. J. Chem.*, 2025, **25**, 1193–1208.

28 S. Manimalathi, J. Priya and D. Madheswari, *Indian J. Chem.*, 2025, **64**, 247–252.

29 S. H. Mahdi and L. K. A. Karem, *Inorg. Chem. Commun.*, 2024, **165**, 112524.

30 R. Priya and P. Metilda, *J. Coord. Chem.*, 2025, **78**, 1981–2007.

31 S. Gunnaz, E. Yildiz, A. T. Oral, F. Yurt, A. Erdem and S. Irisli, *J. Inorg. Biochem.*, 2025, **264**, 112790.

32 S. Yu, K.-N. Truong, M. Siepmann, A. Siiri, C. Schumacher, J. S. Ward and K. Rissanen, *Cryst. Growth Des.*, DOI:10.1021/acs.cgd.2c01162.

33 F. Arshi, S. Bano, S. Parveen, M. Banerjee, N. K. Kushwaha, S. K. Singh, A. Kumar and A. K. Singh, *ChemistrySelect*, 2025, **10**, e202404895.

34 H. Kargar, M. Kubicki, M. Fallah-Mehrjardi, H. R. Zare-Mehrjardi, F. Abyar, K. S. Munawar and M. Ashfaq, *Inorg. Chim. Acta*, 2026, **590**, 122984.

35 M. Gishan, P. Middya, M. G. B. Drew, A. Frontera and S. Chattopadhyay, *RSC Adv.*, 2024, **14**, 30896–30911.

36 A. K. Pal, A. Jaiswal, R. Ravi, K. K. Yadav, D. K. Sahu, R. Kumar and M. Singh, *Polyhedron*, 2024, **264**, 117194.

37 H. Zhang, M. H.-Y. Chan, J. Lam, M.-Y. Leung, L. Wu and V. W.-W. Yam, Org. Chem. Front., DOI:10.1039/d4qo02258k.

38 L. K. Das, P. Bhunia, R. M. Gomila, A. Frontera and A. Ghosh, Crystengcomm, 2023, **25**, 1393–1402.

39 T. Sen, P. Sarkar, S. Sutradhar, D. Das and B. N. Ghosh, *Inorg. Chem. Commun.*, 2024, **170**, 113438.

40 S.-Z. Zhao, L.-W. Chen, H. Zhu, H.-Z. Zhang, C. Liu, C.-Y. Qin, H.-Y. Wang, Y.-H. Li and S. Wang, *Dalton Trans.*, 2025, **54**, 9405–9417.

41 B. Halder, P. Middya, R. M. Gomila, A. Frontera and S. Chattopadhyay, *ACS Omega*, 2024, **9**, 41787–41796.

42 D. Majumdar, A. Frontera, J. E. Philip, B. Gassoumi, S. Burguera, S. Roy and S. Ayachi, *RSC Adv.*, 2025, **16**, 332–352.

43 S. Bera, S. Bhunia, R. M. Gomila, M. G. B. Drew, A. Frontera and S. Chattopadhyay, *RSC Adv.*, 2023, **13**, 29568–29583.

View Article Online
DOI: 10.1039/D6DT00722H

44 R. G. Parr and R. G. Pearson, *J. Am. Chem. Soc.*, 1983, **105**, 7512–7516.

45 S. Parveen, A. Shanmugapriya, B. Saravanakumar, J. J. William and N. Chithra, Next Mater., 2025, **7**, 100339.

46 Z.-Q. Wei, Q.-D. Xu, Y. Liu, Y.-Y. Huang, Y. Li, X.-L. Liu, X.-T. Wu and T.-L. Sheng, *Polyhedron*, 2022, **213**, 115639.

47 A. Altomare, C. Cuocci, C. Giacovazzo, A. Moliterni, R. Rizzi, N. Corriero and A. Falcicchio, *J. Appl. Cryst.*, 2013, **46**, 1238–1244.

48 K. D. M. Harris, M. Tremayne and B. M. Kariuki, *Angew. Chem., Int. Ed.*, 2001, **40**, 1626–1651.

49 A. Yardan and C. Paşa, *Int J Nature Life Sci*, 2024, **8**, 228–240.

50 M. Lago-Silva, M. Fernández-Míguez, R. Rodríguez, E. Quiñoá and F. Freire, *Chem. Soc. Rev.*, 2024, **53**, 793–852.

51 Y. Yao, Q. Ou, K. Wang, H. Peng, F. Fang, Y. Shi, Y. Wang, D. I. Asperilla, Z. Shuai and P. Samorì, *Nat Commun*, 2021, **12**, 3667.

52 A. Altomare, C. Cuocci, C. Giacovazzo, A. Moliterni, R. Rizzi, N. Corriero and A. Falcicchio, *J. Appl. Crystallogr.* 2015, **48**, 598–603.

53 H. M. Rietveld, *J. Appl. Crystallogr.* 1969, **2,** 65–71.

54 F. Neese, WIREs Comput Mol Sci. 2022;12:e1606.10.1002/wcms.1606

View Article Online
DOI: 10.1039/D6DT00722H

55 C. Lee, W. Yang and R. G. Parr, *Phys. Rev. B*, 1988, **37**, 785–789.

56 A. D. Becke, *J. Chem. Phys.*, 1993, **98**, 5648–5652.

57 F. Weigend and R. Ahlrichs, *Phys. Chem. Chem. Phys.*, 2005, **7**, 3297–3305.

58 S. Grimme, J. Antony, S. Ehrlich and H. Krieg, *J. Chem. Phys.*, 2010, **132**, 154104.

59 S. Grimme, S. Ehrlich and L. Goerigk, *J. Comput. Chem.*, 2011, **32**, 1456–1465.

60 F. Neese, F. Wennmohs, A. Hansen and U. Becker, *Chem. Phys.*, 2009, **356**, 98–109.

61 T. Lu and F. Chen, *J. Comput. Chem.*, 2012, **33**, 580–592.

62 R. F. W. Bader, *Chem. Rev.*, 1991, **91**, 893–928.

63 E. Espinosa, E. Molins and C. Lecomte, *Chem. Phys. Lett.*, 1998, **285**, 170–173.

64 E. R. Johnson, S. Keinan, P. Mori-Sánchez, J. Contreras-García, A. J. Cohen and W. Yang, *J. Am. Chem. Soc.*, 2010, **132**, 6498–6506.

65 K. Momma and F. Izumi, *J Appl Cryst*, 2011, **44**, 1272–1276.

View Article Online
DOI: 10.1039/D6DT00722H

Data availability

The datasets generated and analyzed during the current study are available within the manuscript and its Electronic Supplementary Information (ESI) file. The crystallographic data for the synthesized complexes have been deposited at the Cambridge Crystallographic Data Centre (CCDC) under the accession numbers; 2534339, 2534340, 2534341, 2534343, 2535251, 2536167. Copies of these data can be obtained free of charge via www.ccdc.cam.ac.uk/data_request/cif. Additional raw computational data, including optimized geometries, input coordinates, and topological analyses, are available from the corresponding author upon reasonable request.